Pursuant to the DOE Public Access Plan, this document represents the authors' peer-reviewed, accepted manuscript. The published version of the article is available from the relevant publisher.

ACS APPLIED MATERIALS & INTERFACES

Subscriber access provided by National Renewable Energy Laboratory Library

Article

Junction Quality of SnO_2-Based Perovskite Solar Cells Investigated by Nanometer-Scale Electrical Potential Profiling

Chuanxiao Xiao, Changlei Wang, Weijun Ke, Brian Gorman,
Jichun Ye, Chun-Sheng Jiang, Yanfa Yan, and Mowafak Al-Jassim

ACS Appl. Mater. Interfaces, **Just Accepted Manuscript** • DOI: 10.1021/acsami.7b08582 • Publication Date (Web): 13 Oct 2017

Downloaded from http://pubs.acs.org on October 18, 2017

Just Accepted

"Just Accepted" manuscripts have been peer-reviewed and accepted for publication. They are posted online prior to technical editing, formatting for publication and author proofing. The American Chemical Society provides "Just Accepted" as a free service to the research community to expedite the dissemination of scientific material as soon as possible after acceptance. "Just Accepted" manuscripts appear in full in PDF format accompanied by an HTML abstract. "Just Accepted" manuscripts have been fully peer reviewed, but should not be considered the official version of record. They are accessible to all readers and citable by the Digital Object Identifier (DOI®). "Just Accepted" is an optional service offered to authors. Therefore, the "Just Accepted" Web site may not include all articles that will be published in the journal. After a manuscript is technically edited and formatted, it will be removed from the "Just Accepted" Web site and published as an ASAP article. Note that technical editing may introduce minor changes to the manuscript text and/or graphics which could affect content, and all legal disclaimers and ethical guidelines that apply to the journal pertain. ACS cannot be held responsible for errors or consequences arising from the use of information contained in these "Just Accepted" manuscripts.

ACS Publications

ACS Applied Materials & Interfaces is published by the American Chemical Society.
1155 Sixteenth Street N.W., Washington, DC 20036

Published by American Chemical Society. Copyright © American Chemical Society. However, no copyright claim is made to original U.S. Government works, or works produced by employees of any Commonwealth realm Crown government in the course of their duties.

Junction Quality of SnO_2-Based Perovskite Solar Cells Investigated by Nanometer-Scale Electrical Potential Profiling

Chuanxiao Xiao,[1,2†] Changlei Wang,[3†] Weijun Ke,[3] Brian P. Gorman,[2] Jichun Ye,[4] Chun-sheng Jiang,[1*]
Yanfa Yan,[3*] and Mowafak M. Al-Jassim[1]

[1] National Renewable Energy Laboratory, Golden, CO 80401 USA

[2] Colorado School of Mines, Golden, CO 80401 USA

[3] The University of Toledo, Toledo, OH 43606 USA

[4] Ningbo Institute of Industrial Technology, Chinese Academy of Science, Ningbo, China

[†] These authors contributed equally to this work
[*] Correspondence should be addressed to: chun.sheng.jiang@nrel.gov; yanfa.yan@utoledo.edu.

Abstract: Electron-selective layers (ESLs) and hole-selective layers (HSLs) are critical in high-efficiency organic-inorganic lead halide perovskite (PS) solar cells for charge-carrier transport, separation, and collection. We developed a procedure to assess the quality of the ESL/PS junction by measuring potential distribution on cross-section of SnO_2-based perovskite solar cells using Kelvin probe force microscopy. Using the potential profiling, we compared three types of cells made of different ESLs but otherwise having identical device structure: 1) cells with PS deposited directly on bare fluorine-doped SnO_2 (FTO)-coated glass; 2) cells with an intrinsic SnO_2 thin layer on the top of FTO as an effective ESL; and 3) cells with the SnO_2 ESL and adding a self-assembled monolayer (SAM) of fullerene. The results reveal two major potential drops or electric fields at the ESL/PS and PS/HSL interfaces. The electric-field ratio between the ESL/PS and PS/HSL interfaces increased in devices as follows: FTO < SnO_2-ESL < SnO_2+SAM; this sequence explains the improvements of fill factor (FF) and open-circuit voltage (V_{oc}). The improvement of FF from the FTO to SnO_2-ESL cells may result from the reduction in voltage lose at the PS/HSL back interface and the improvement of V_{oc} from the prevention of hole recombination at the ESL/PS front interface. The further improvements with adding a SAM is caused by the defect passivation at the ESL/PS interface, and hence, improvement of the junction quality. These nanoelectrical findings suggest possibilities for improving the device performance by further optimizing the SnO_2-based ESL material quality and the ESL/PS interface.

Keywords: Kelvin probe force microscopy, junction quality, perovskite solar cell, electron-selective layer, interface, nanometer-scale, potential profile.

1. Introduction

Organic-inorganic hybrid lead halide perovskite (PS) solar cells have developed rapidly, now reaching a conversion efficiency of 22.1%.[1] In the solar cell structure, electron-selective layers (ESLs) and hole-selective layers (HSLs) are critical for the transport, separation, and collection of charge carriers. The most common device architecture uses titanium dioxide (TiO_2) as the ESL.[2–6] However, it has been argued that TiO_2 may not be the ultimate ESL material because of band misalignment with PS and relatively low electron mobility.[7–9] In fact, other oxides, such as ZnO and SnO_2, have similar or ever better optical and electrical properties than TiO_2.[9–12] In particular, SnO_2-based solar cells are continually showing great potential and have achieved high efficiencies up to 21% to date.[12–21] Ideally, the better band alignment of SnO_2 and PS[9] and higher electron mobility provide the possibility of achieving better performance than that of TiO_2-based cells; however, the champion cell still uses TiO_2 as ESL. The inferior performance of cells made of SnO_2 ESL may not be due to its intrinsic material properties. Indeed, steady-state photoluminescence showed a quenching effect, and time-resolved photoluminescence showed additional reduced lifetime with PS deposited on SnO_2 rather than on TiO_2—indicating more efficient electron transfer from PS to SnO_2 layer than PS to TiO_2, and thus, great potential for future improvement.[17,21,22] Rather, subpar performance is likely due to issues of processing optimization, which causes poor material quality, junction quality, and interface defect states. A deeper understanding of the interface electronic properties between the ESL and PS is therefore required to optimize alternative ESL materials.

This paper describes a procedure we developed to investigate the interface between a SnO_2-based ESL and PS absorber, where we do potential profiling across the interface using Kelvin probe force microscopy (KPFM).[23–26] The applied bias voltage to the devices drops at both sides of the front interface of ESL/PS and back interface of PS/HSL. By comparing the electric-field distribution at both the front and back interfaces with changes to the SnO_2-based ESL structure, we observed improvements of the front-junction quality by adding an intrinsic SnO_2 ESL and further improvement by adding a self-assembled monolayer (SAM) layer. These results explain the gains in cell performance from the perspective of junction quality.

2. Experiment

Three types of PS cells[12–16] (**Figure 1**) were subjected to potential profiling: 1) Cells without an ESL, where the PS layer was deposited directly on a bare TEC15 substrate, a soda-lime glass coated with fluorine-doped SnO_2 (FTO). FTO is a highly conductive n-type semiconductor that serves as the ESL. Because photo-generated holes in the PS active layer can diffuse to the ESL/PS interface and recombine with the high concentration of electrons in the FTO right at the FTO/PS interface, this device has no effective ESL or hole-blocking effect.[12] 2) Cells with an extra layer of intrinsic SnO_2 as an alternative ESL with effects of both electron-transport and hole-blocking.[13,14] Because of the low density of electrons in this layer, recombination of holes diffused to the SnO_2/PS interface can effectively be prevented. 3) Cells with a self-assembled monolayer of fullerene deposited on the top of intrinsic SnO_2.[15,16]

The intrinsic SnO_2 layer was made by two processes of either solution or atomic layer deposition (ALD). Solution-based SnO_2 was prepared by a low temperature solution process; the solution of 0.1 mol L^{-1} $SnCl_2$ (Alfa, anhydrous 99.9985%) dissolved in ethanol was spin-coated on clean FTO substrates (Pilkington, NSG TEC-15) with a spin rate of 2000 rpm for 30 s, followed by annealing at 185 ^{o}C for 1 h. These substrates were cleaned using plasma etching for 15 min before PS deposition. The plasma-enhanced ALD processed SnO_2 layer was deposited on the FTO substrates using an equipment of Ensure Scientific Group AutoALD-PE V2.0 equipped with a plasma generator. Tetrakis(dimethylamino)-tin(IV) (99%, TDMA-Sn, Strem Chemicals Inc.) was used as the Sn precursor. Oxygen and argon are used as oxidizer and carrier gases, respectively. The temperature of the reaction is fixed at 100 ^{o}C during the deposition process. The SnO_2 films are annealed on a 100 ^{o}C hot plate for 1 hour. C60-SAM was spin-coated by dissolving C60-SAM solution in chlorobenzene with concentration of 4 mg/mL at 3000 rpm for 30 s. Lead iodide (PbI_2, Alfa Aesar, 99.9985%), methylammonium iodide (MAI, Dyesol), formamidinium iodide (FAI, Dyesol), lead thiocyanate ($Pb(SCN)_2$, Sigma-Aldrich, 99.5%), dimethyl sulfoxide (DMSO, Sigma-Aldrich, 99.8%) and N,N-dimethylformamide (DMF, Sigma-Aldrich, 99.8%) were used without further purification. The perovskite precursor solution was prepared using a Lewis acid-base adduct approach with the mixture of MAI, FAI, PbI_2, and DMSO in DMF, where the molar ratio of DMSO and PbI_2 is 1:1. A 45% by weight precursor solution of $MA_{0.7}FA_{0.3}PbI_3$ was prepared with PbI_2, MAI, FAI, $Pb(SCN)_2$ and DMSO (molar ratio=1:0.7:0.3:0.02:1) in DMF. The solution was stirred for 12 h on a 60 ^{o}C hot plate before deposition. The PS precursor solution was spin-coated on the ESL first at 500 rpm for 3 s, and then at 4000 rpm for 60 s using a fast deposition-crystallization technique with diethyl ether as the anti-solvent agent. After spin coating, the PS film was annealed at 65 °C for 2 min and then 100 °C for 5 min. All of these processes were carried out in a N_2 filled glove box. 2,2',7,7'-tetrakis(N,N'-di-p-methoxyphenylamine)-9,9'-spirobifluorene (Spiro-OMeTAD) was used as the hole transport material and deposited on the PS film at 2000 rpm for 60 s. The Spiro-OMeTAD was co-doped using Li-bis-(trifluoromethanesulfonyl) imide (Li-TFSI) and Co-TFSI. The Spiro-OMeTAD solution was prepared by dissolving 72.3 mg Spiro-OMeTAD (Shenzhen Feiming Science and Technology Co., Ltd., 99.0%) in 1 mL chlorobenzene with 28 μL 4-tert-butylpyridine (Sigma-Aldrich, 96%), 18 μL Li-TFSI (Sigma-Aldrich, 99.95%) (520 mg/mL in acetonitrile) and 18 μL Co(II)–TFSI salt (FK102, Dyesol) (300 mg/mL in acetonitrile). A layer of 80 nm gold (Au) was then deposited on the top using thermal evaporation.

The devices were cleaved from the film side to expose the cross section, and no further treatment (e.g., polishing, ion milling) was applied to the cross-sectional sample so as to avoid complications and artifacts from the treatment (See **Fig. S1** for details of cleaving method and the description in supplemental materials). In the KPFM measurement, the FTO side or front side of the device was grounded, and bias voltage was applied from the back contact of the devices. The measurements were performed in an Ar-filled glove box with water and oxygen content < 0.1 ppm to mitigate possible degradation of the devices.

KPFM is based on the noncontact mode of an atomic force microscope (AFM). By probing and nullifying the Coulomb force between the probe (Nanosensor PPP-EFM) and the sample, KPFM measures the contact potential difference between the probe and sample. The workfunction of the probe remains unchanged, and the electrostatic potential on the sample's surface is mapped at a spatial resolution of ~30 nm and a potential resolution of ~10 mV.[23] Topographic and electrical images were collected simultaneously during the probe scanning. In KPFM measurements, the surface potential is often dominated by electrical charges trapped on the cross-sectional surface, which is nonuniform across the surface and depends on the cleaving of the sample. To avoid the effect of surface charge and to "see" the potential distribution in the device bulk, we applied a bias voltage to a working device and measured the changes of surface potential with the bias voltage. Because the surface charge configuration should not change with the small bias voltage of 0–2 V, the measured change of the surface potential is about identical with the potential change in the bulk. In this way, we determined the potential change in the bulk by measuring the surface potential change,[23–26] which is the device characteristic we aim to investigate in this paper.

KPFM measurements were performed with varying bias voltage from -1.5 V (reverse bias) to +0.5 V (forward bias) on the same area. The quality of the p-n junction can be assessed by the current leak or equivalent shunt resistance under reverse bias voltages through measuring voltage drop at the junction. All KPFM data were collected in dark, no photo-induced current during the measurements. For every set of data, we find an area with a relatively flat surface (< 50-nm corrugation) on the cross section to eliminate the cross-talk of topography and potential signals. We examined two different locations on two samples for each type of cells to ensure reliable results. The line potential profiles were averaged from 64 scan lines of potential images. The relatively slow scan—each image takes about 3 min—is to ensure data quality, and no plausible ion migration was observed in the small bias voltages. To minimize the effect of ion migration, if any, we altered the forward and reverse voltages for data acquisition by taking images in the order of 0 V, -0.5 V, +0.5 V, -1 V, and so on. We also used a much faster scan rate (30 s per image) and found no significant difference except for the data noise level or quality. Scanning electron microscopy (SEM) images identified the multiple layers in the device and their interfaces.

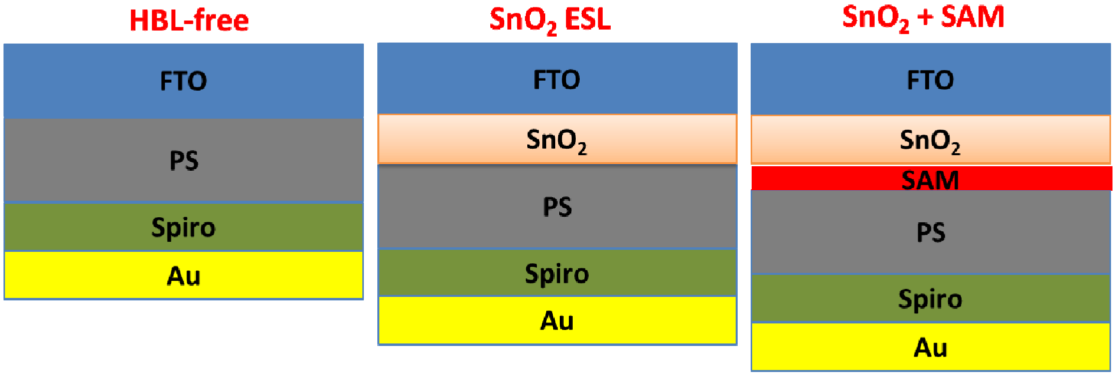

Figure 1. Schematic of PS cell structures in this study.

3. Results and Discussion

Photocurrent density-voltage (J-V) curves and device performance parameters of the solar cells used in this work are shown in **Figure 2** and **Table 1**, respectively. The three types of cells—made on the bare FTO (also noted as ESL-free cell), intrinsic SnO_2 ESL, and SnO_2 adding a SAM—all have state-of-the-art efficiencies. The PS active layer and PS/Spiro back interface should be identical among the cells; the only variation is the ESL and ESL/PS interface. The cell with intrinsic SnO_2 is significantly improved and shows less hysteresis, compared with the HBL-free cell. In reverse scan (i.e., from V_{oc} to J_{sc}), the two devices have an ~20% difference in conversion efficiencies (SnO_2: 17.78% and ESL-free: 13.91%), which results from differences of ~8% in fill factor (FF) (73.85% and 68.10%), 12% in V_{oc} (1.07 and 0.94 V), and 3% in J_{sc} (22.40 and 21.64 mA/cm^2). In forward scan (i.e., from J_{sc} to V_{oc}), the two devices have an ~40% difference in conversion efficiencies (SnO_2: 16.33% and ESL-free: 9.85%), which results from differences of ~18% in FF (70.68% and 58.08%), 24% in V_{oc} (1.03 and 0.78 V), and 3% in J_{sc} (22.4 and 21.62 mA/cm^2).

The SnO_2 layer was deposited by either solution-based spin coating or atomic layer deposition (ALD). We did not observe a significant difference in the best devices between these two methods. However, ALD has better reproducibility than spin coating, because ALD is well controllable when depositing such a thin film (~15 nm).[9,16,27] The ALD SnO_2 adding SAM has the best efficiency of 19.28% (19.25%) among the three cells, with a V_{oc} of 1.09 V (1.09 V), a J_{sc} of 23.20 mA/cm^2 (23.20 mA/cm^2), and a FF of 76.39% (76.35%) measured under reverse (forward) voltage scan. Adding the SAM layer mainly improved FF (from 73.85% to 76.39% under reverse scan, and from 70.68% to 76.35% under forward scan); the V_{oc} and J_{sc} values are similar to the cell with intrinsic SnO_2 ESL. SAM is expected to passivate interface trap states and enhance charge transfer.[15,22,28,29] Recent publications[30–34] found that PS and metal oxides can react and form an unwanted MAI- or PbI_2-rich interface, which is an electron extraction barrier. It is possible that the SAM can suppress or minimize such reactions to form a cleaner interface. The statistical results of 94 PS cells performance are shown in **Fig. S2** and **Table S1**. And the stable output of typical cells of each type is shown in **Fig. S3**, indicating significant different performance for these cells. **Fig. S4** showed the representative external quantum efficiency (EQE) curves of the three types of cells, and the calculated J_{sc} under a 100 mW cm^{-2} AM1.5 spectrum. The EQE results clearly showed change at 600-800 nm, which suggests higher recombination of the device without SnO_2 ESL. In general, this recombination loss is introduced by less-than-ideal collection efficiencies of photo-generated carriers. The longer the wavelength has the deeper the generation of carriers, hence the higher the possibility of recombination.[35] The light dependence of Voc curves are shown in **Fig. S5**, indicating a reduced trap-assist recombination by the reduction of ideality factor from 1.76 (ESL-free), 1.54 (SnO_2 ESL) to 1.38 (SnO_2+SAM). The dark I-V curves in **Fig. S6** showed large decrease in current from the ESL-free to SnO_2 ESL cells and further slight decrease in the SnO_2+SAM cell. These performance parameters suggest a difference in junction quality and a large difference in carrier transport across the device, including barriers in the front junction and back interface. The superior V_{oc} of the low-temperature, solution-processed SnO_2 device is not surprising because SnO_2 has a barrier-free conduction-band alignment, whereas the device with the most commonly used TiO_2 ESL has an ~80-meV band misalignment.[9] The hysteresis effect is also decreased substantially by adding SnO_2 and SAM, which will not be discussed in this paper, as the focus here is p-n junction quality.

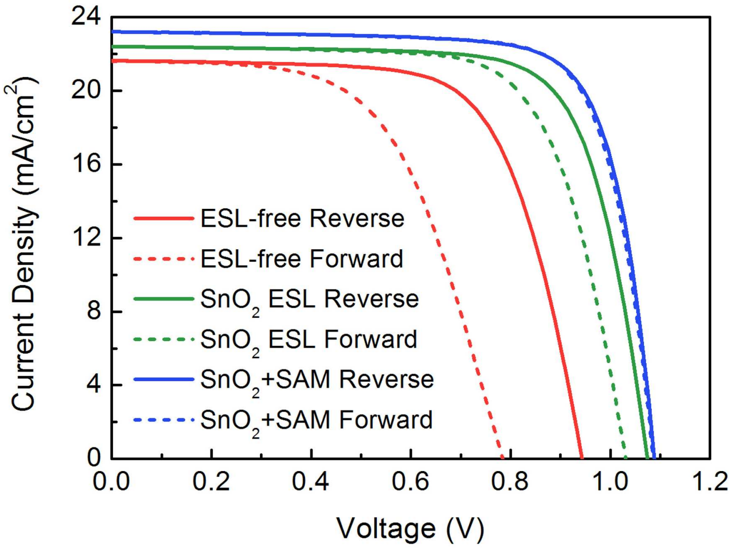

Figure 2. J-V curves of the three types of ESL cells subjected to the potential profiling study.

Table 1. Photovoltaic Performance Parameters of the Three Types of Cells

Cell Type	Scan Direction	V_{OC} (V)	J_{SC} (mA/cm^2)	FF (%)	Eff. (%)
ESL-free	Reverse	0.94	21.64	68.10	13.91
	Forward	0.78	21.62	58.08	9.85
SnO_2 ESL	Reverse	1.07	22.40	73.85	17.78
	Forward	1.03	22.40	70.68	16.33
SnO_2 + SAM	Reverse	1.09	23.20	76.39	19.28
	Forward	1.09	23.20	76.35	19.25

Figure 3 shows potential-profiling results across the FTO ESL-free cell. Figure 3(a) is an SEM image of the device with an FTO layer thickness of 380 nm, PS layer of 630 nm, HSL of 200 nm. The potential line profiles [Fig. 3(b)] were averaged from 64 scan lines of potential images (Supplemental **Fig. S7**) along the device lateral direction to enhance the signal/noise ratio. The 0-V potential profile was subtracted from the potential profiles taken at the various bias voltages, and the results are potential changes from the 0-V profile [Fig. 3(c)]. First derivatives of the potential profiles are taken to get electric field differences [Fig. 3(d)]. On the ESL-free device, two large electric fields on both the ESL/PS and PS/Spiro interfaces were observed, but not in the middle of the PS layer. These electric-field profiles indicate a p-n junction-like cell with the main junction at the ESL/PS interface and a significant potential barrier at the PS/Spiro interface; but they are not favorable to the widely discussed p-i-n-like junction or excitonic device. If it was a p-i-n junction or an excitonic device, the electric field would mainly be located across the PS layer.

The large electric-field peak at the PS/HSL back interface suggests a poor main junction at the ESL/PS interface. With a bias voltage applied to the device—because the electric current through the device or through the front junction and back barrier must be the same—if there is a significant voltage drop at the back side, the voltage drop at the front junction must be reduced. This indicates a reduced equivalent shunt resistance in the front junction, resulting from poor junction quality or increased reverse saturation current J_0 and/or diode ideality factor. Therefore, the front junction can be assessed using the ratio of voltage drop between the front and back sides as identified from the electric-field profile. The back PS/HSL barrier should be identical in the three types of cells, so we use this procedure to compare their front-junction quality.

In our previous work,[23] we found that all of the voltage drop in TiO_2 ESL-based PS devices occurred on the front junction, but neither on the back PS/Spiro interface nor in the PS active layer. We concluded that the PS device is a normal p-n junction cell similar to the polycrystalline inorganic solar cells such as CdTe and $Cu(In,Ga)Se_2$, and the free p-type carrier in the PS absorber was in ~$10^{16}/cm^3$ order. Differing from the previous work,[23] we found a large electric peak or voltage drop at the PS/Spiro back interface in the SnO_2 ESL-based devices. This indicates a poorer SnO_2-based junction quality, and thus, a great opportunity for further improving the SnO_2-based junction or interface. Further, we developed a novel characterization for the front junction diode quality by comparing the electric field peaks between the front ESL/PS junction and PS/Spiro back interface with varying the ESL layer material and processing, which provides an unparalleled junction evaluation, as detailed later.

On the potential profiles (Fig. 3b), one sees a change in the potential at TCO with varying the bias voltage, while TCO of the device was grounded during the KPFM measurement. Two reasons can be responsible for the potential at TCO. (1) Because cleaving the sample cross-section would create shunts and decrease the shunt resistance, current under a V_b is larger than an actual device with the same bias voltage. This changes the potential at TCO because of the series resistance of TCO and contact resistance. (2) The other is the contribution of interaction of probe cantilever with the sample regions other than under the probe tip. When a bias is applied to the back contact and the tip is on TCO, cantilever can “sense” the voltage at the device stack in some degree.

The same experiment procedure was applied to the SnO_2-ESL cells and the results are shown in **Figure 4,** the corresponding potential images are showed in Supplemental **Fig. S8**. Figure 4(a) shows an SEM image of the SnO_2-ESL cell; the structure is similar to the ESL-free layer except for the ~15-nm additional intrinsic SnO_2 layer. The SnO_2-ESL and ESL-free cells were fabricated in the same batch so that all the layer structures other than the intrinsic SnO_2 should be identical. Figure 4(b) shows the potential profiles across the device under the various bias voltages. Figures 4(c) and 4(d) show the electrical potential and field differences from the 0-V ones, respectively. Similarly, there are two electric-field peaks at the SnO_2/PS and PS/Spiro interfaces [Fig. 4(d)]. However, the main potential drop or the electric field occurs over the interface between n-type SnO_2 ESL and the p-type PS absorber layer. There is still a peak at the PS/Spiro interface, but it is significantly smaller when compared with the ESL-free cell.

The degree of voltage drop at the ESL/PS junction relative to that at PS/Spiro is significantly larger in the SnO_2 device than in the ESL-free device. This result indicates a better diode quality factor of the ESL/PS junction and/or a smaller J_0 of the SnO_2 device than the ESL-free device, which is consistent with the V_{oc} difference of the two devices. In other words, if the front junction is better formed and the reverse current flowing through the junction is reduced, then the potential/voltage drop at the backside interface will decrease. In this case, the two junctions will compete less, which leads to better performance. This highlights that SnO_2 can work as an effective hole-blocking layer because it prevents photo-generated hole recombination at the FTO/PS interface. The J_{sc} values of the two devices are similar, which indicates that FTO and FTO/SnO_2 can both work as good electron-transport layers.

On the other hand, the smaller voltage drop at the PS/Spiro interface of the SnO_2 device is consistent with the pronounced FF and V_{oc} gain. In fact, FF should be a significantly affected parameter by this "back-contact" voltage drop. This is because voltage loss at the back side of the device greatly affects the voltage at the maximum power output point of a J-V curve, and hence, greatly affects FF. It is worth mentioning that we examined the cells with both solution-based spin-coating and ALD SnO_2 layers. ALD SnO_2 is expected to be better crystallized and less defective material, but we observed no significant difference of KPFM results on the cells with similar performances. This indicates that the SnO_2 ESL cells in this study are representative and independent from the deposition methods. However, this does not necessarily mean that cells with intrinsic SnO_2 could not be improved; with a better SnO_2/PS interface, we would expect a higher performance device.

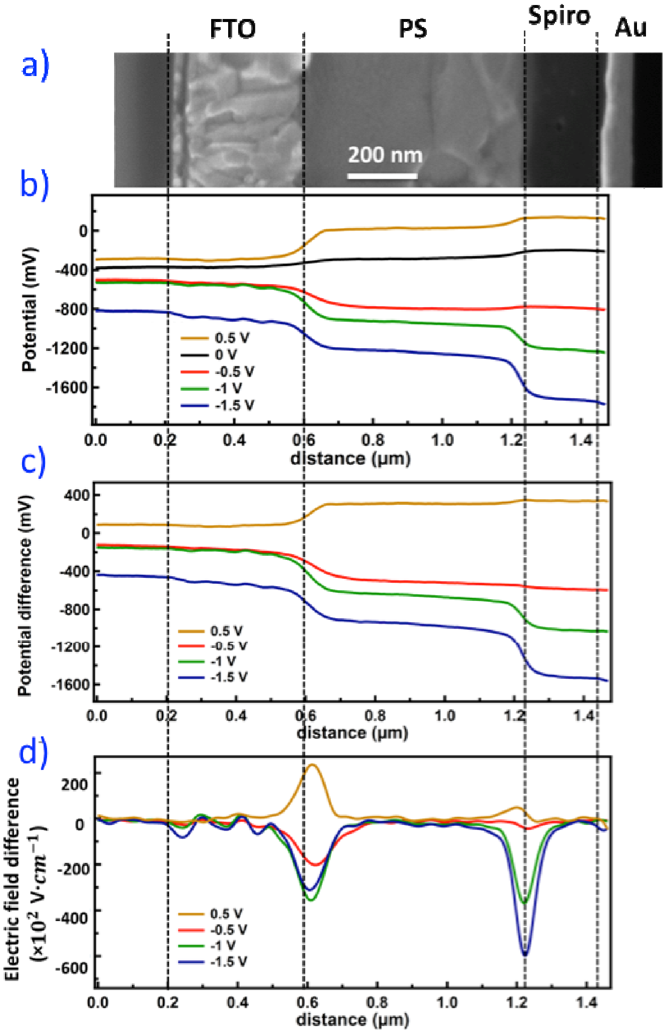

Figure 3. (a) An SEM image showing layer structure of the ESL-free cell; (b) Potential profilings across the ESL-free cell under different bias voltages; (c) Potential differences across the ESL-free cell subtracted by the 0-V curve; and (d) Electric-field difference across the ESL-free cell, taken by the first derivative in (c).

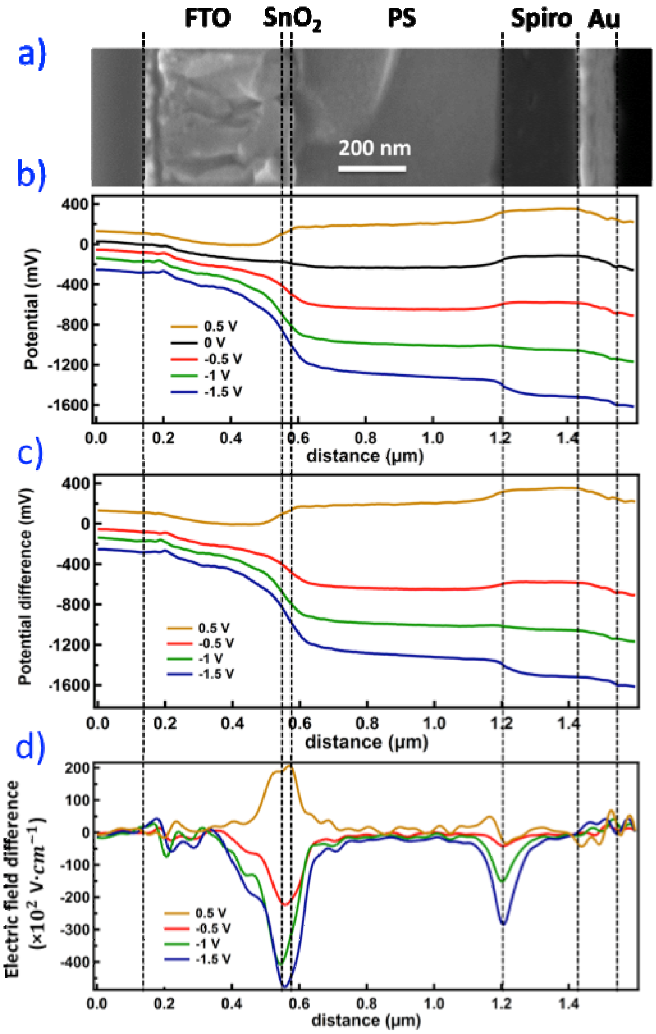

Figure 4. (a) An SEM image showing layer structure of the SnO_2-ESL cell; (b) Potential profilings across the SnO_2-ESL cell under different bias voltages; (c) Potential differences across the SnO_2-ESL cell subtracted by the 0-V curve; and (d) Electric-field difference across the SnO_2-ESL cell, taken by the first derivative in (c).

SAM is reported to improve the cell performance by promoting charge extraction of ESL, passivating the ESL/PS interface defect states,[15,22,28,29]or making a cleaner interface of ESL/PS.[30–34] The reduction in defective sites at the SnO_2/PS interface is expected to lead to a lower nonradiative recombination rate and thus improve the junction quality. **Figure 5** shows the potential-profiling results across a cell with SnO_2 and SAM. The corresponding potential images are showed in Supplemental **Fig. S9.** The SEM image [Fig. 5(a)] is similar to that without the SAM layer [Fig. 4(a)] because the SAM layer is too thin to be resolved in the SEM image. Similar to the two cells above, Fig. 5(b) shows the potential profiles under the various bias voltages; Figure 5(c) shows the potential change with bias voltages; and Fig. 5(d) shows the electric-field changes. As expected, the KPFM results show the largest peak ratio of ESL/PS versus PS/HSL among the three types of SnO_2-based cells. The main potential drop is at the p-n junction formed by SnO_2/SAM/PS, but the peak at PS/Spiro (relative scale) is smaller than the SnO_2 cell without SAM. As discussed above, because the electrical current flowing through all the regions must be the same in the steady state, the voltage drop at the PS/Spiro interface is determined by the ratio between the equivalent shunt resistance at the interface and the sum of all other equivalence resistance in the circuit loop including the front junction, the series resistance, and contact resistance etc. Although the back contact materials are the same among the three devices, the voltage drop at the backside is different, because the total equivalent shunt resistance and the shunt resistance of the front junction are different among the three devices. This is how we can assess the front-junction quality by comparing the voltage drop ratio among the devices. The smaller peak at the PS/Spiro side indicates a smaller J_0 and a better interface quality of SnO_2/SAM/PS than SnO_2/PS. We did same experiments on two different locations of two samples for each type of cells to ensure reliable results, another set of representative potential-profiling results are showed in Supplemental **Fig. S10-S12**.

Table 2 lists the ratios of the two peak heights or electric field strength under reverse bias of -1.5 V for the three types of cells. The ESL/PS interface is noted as “Peak 1” and the PS/Spiro interface as “Peak 2.” For the four sets of data we examined on each type of cells, the ESL-free cell has an average Peak 1/Peak 2 ratio of 0.39; the SnO_2 cell has an average ratio of 1.65; and the SnO_2+SAM cell a ratio of 3.25. We examine the electric field peak ratio under a reverse bias voltage rather than under a forward bias, because the data under reverse are more reliable. Electric current under forward bias is relatively large, which generally leads to bad data quality and the potential profiling is not stable for a time period during the measurement with a large current. These KPFM results are consistent with cell performances; the larger the peak1/peak2 ratio, the better the front-junction quality, the lower the voltage loss at the back side, and the better the FF and V_{oc}. Most likely, the improvement by adding the SAM layer is because of defect-state passivation at the SnO_2/PS interface. The SAM layer may also promote charge extraction.[28,29,36]However, its effect may be minor because the layer is very thin and carriers can tunnel through it.

The junction quality assessment results (Table 2) as evaluated by the equivalent shunt resistance through the measurement of voltage drop are consistent with the device performance parameters (Table 1) by changing the SnO_2-based ESL processing. This consistency also showed up with the I-V hysteresis as shown in Fig. 2, the larger the Peak 1/Peak 2 ratio, the smaller the hysteresis. In another note, however, this voltage drop measured by potential profiling cannot deduce detailed mechanisms of the junction improvement by changing the SnO_2-based ESL processing, such as interface passivation, band alignment, or prevention of interface reaction etc.

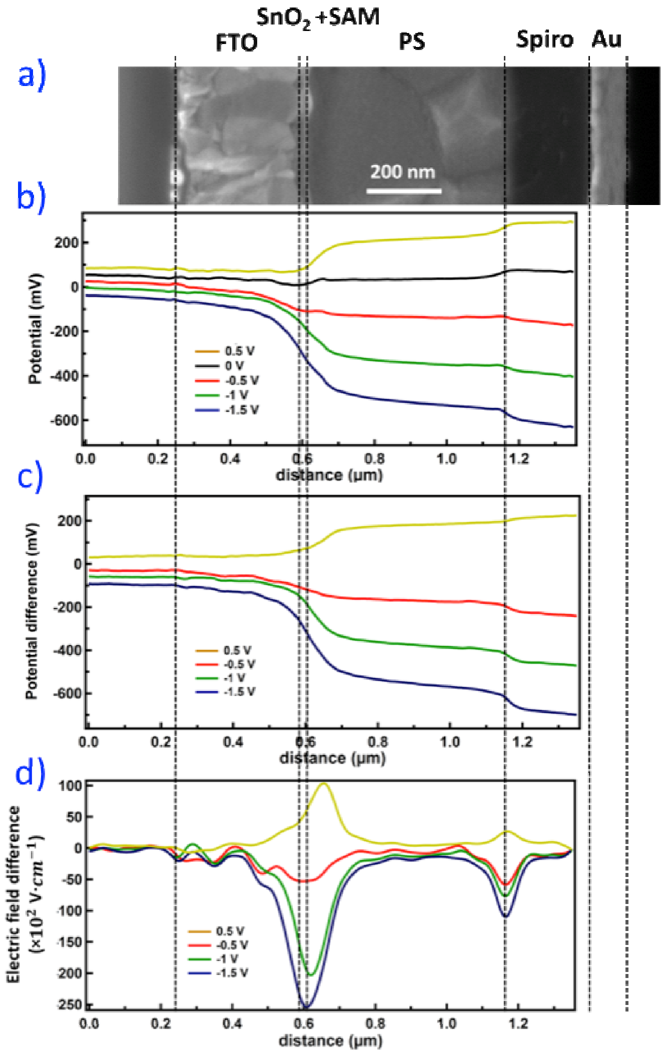

Figure 5. (a) An SEM image showing layer structure of the SnO_2+SAM cell; (b) Potential profilings across the SnO_2+SAM cell under different bias voltages; (c) Potential differences across the SnO_2+SAM cell subtracted by the 0-V curve; and (d) Electric-field difference across the SnO_2+SAM cell, taken by the first derivative in (c).

Table 2. Peak Ratios of KPFM Electric Field at the ESL/PS and PS/HSL Interfaces

Cell Structure	Experiment set #	Peak1 Intensity (a.u.)	Peak2 Intensity (a.u.)	Peak1/Peak2 Ratio	Peak1/Peak2 Ratio average
ESL-free	1	310	600	0.52	0.39
	2	574	1438	0.40	
	3	135	418	0.32	
	4	39	122	0.32	
SnO_2 ESL	1	476	284	1.68	1.65
	2	324	194	1.67	
	3	131	77	1.70	
	4	382	245	1.56	
SnO_2 + SAM	1	254	110	2.31	3.25
	2	398	104	3.83	
	3	278	55	5.05	
	4	207	114	1.82	

4. Conclusion

We investigated the junction electrical property of SnO_2-based PS solar cells by profiling the electrical potential across the devices in nm resolutions using the nanoelectrical probe of KPFM. We further developed a procedure to assess the ESL/PS junction quality by comparing the electric-field ratio at the front ESL/PS and back PS/HSL interfaces between the cells with changing only the ESL. We found significant differences in the electric-field ratio in the increasing order of ESL-free < SnO_2-ESL < SnO_2 + SAM, which is consistent with the FF and V_{oc} gains and I-V hysteresis reductions resulting from the ESL improvements. The correlation of these KPFM results with cell performance is understood in terms of ESL/PS front-junction quality and voltage loss at the PS/HSL back interface. The ESL-free cell has the largest relative potential drop at the PS/Spiro interface among the three cells, suggesting a relatively poor p-n junction at the FTO/PS interface, which leads to a poor V_{oc}, and a large voltage loss at the back side, which leads to a poor FF. The increase of the electric-field ratio by adding the SnO_2-ESL proposes, on one hand, improved junction quality by preventing photo-generated hole recombination, and, on another hand, a significant reduction in voltage loss at the back interface. The further increase of electric-field ratio between the front and back interfaces by adding a SAM agrees with effectively passivating defect states at the ESL/PS interface. The procedure of potential profiling and comparing the electric-field ratio provides novel nanoelectrical characterization related directly to cell performance. This characterization also has a broad implication for an unparalleled junction quality evaluation for wide photodiode-based optoelectronic devices. The results of PS devices highlight possible further improvement of the ESL material and interface/junction quality.

ACKNOWLEDGEMENTS

The authors thank Bobby To for taking SEM images. C.X thanks Dr. Zhen Li (National Renewable Energy Laboratory, USA) for fruitful discussion. This work was supported by the U.S. Department of Energy under Contract No. DE-AC36-08GO28308 with the National Renewable Energy Laboratory.

Supporting Information

Method to cleave the sample, sketch of how to cleave the sample to expose cross section, statistical performance of the three types of cells, table of statistical results of performance, stable output of the three types of cells, EQE, light dependence of Voc, dark I-V, KPFM mapping of the cells, extra potential profiling of the three types of cells.

5. References

(1) NREL efficiency chart. http://www.nrel.gov/pv/assets/images/efficiency_chart.jpg.

(2) Jeon, N. J.; Noh, J. H.; Kim, Y. C.; Yang, W. S.; Ryu, S.; Seok, S. I. Solvent Engineering for High-Performance Inorganic–organic Hybrid Perovskite Solar Cells. *Nat. Mater.* **2014**, *13* (9), 897–903.

(3) Yang, W. S.; Noh, J. H.; Jeon, N. J.; Kim, Y. C.; Ryu, S.; Seo, J.; Seok, S. I. High-Performance Photovoltaic Perovskite Layers Fabricated through Intramolecular Exchange. *Science* **2015**, *348* (6240), 1234–1237.

(4) Liu, M.; Johnston, M. B.; Snaith, H. J. Efficient Planar Heterojunction Perovskite Solar Cells by Vapour Deposition. *Nature* **2013**, *501* (7467), 395–398.

(5) Green, M. A.; Ho-Baillie, A.; Snaith, H. J. The Emergence of Perovskite Solar Cells. *Nat. Photonics* **2014**, *8* (7), 506–514.

(6) Zhou, H.; Chen, Q.; Li, G.; Luo, S.; Song, T.; Duan, H.-S.; Hong, Z.; You, J.; Liu, Y.; Yang, Y. Photovoltaics. Interface Engineering of Highly Efficient Perovskite Solar Cells. *Science* **2014**, *345* (6196), 542–546.

(7) Tiwana, P.; Docampo, P.; Johnston, M. B.; Snaith, H. J.; Herz, L. M. Electron Mobility and Injection Dynamics in Mesoporous ZnO, SnO_2, and TiO_2 Films Used in Dye-Sensitized Solar Cells. *ACS Nano* **2011**, *5* (6), 5158–5166.

(8) Snaith, H. J.; Ducati, C. SnO_2-Based Dye-Sensitized Hybrid Solar Cells Exhibiting Near Unity Absorbed Photon-to-Electron Conversion Efficiency. *Nano Lett.* **2010**, *10* (4), 1259–1265.

(9) Baena, J. P. C.; Steier, L.; Tress, W.; Saliba, M.; Neutzner, S.; Matsui, T.; Giordano, F.; Jesper Jacobsson, T.; Kandada, A. R. S.; M. Zakeeruddin, S.; Petrozza, A.; Abate, A.; Khaja Nazeeruddin, M.; Grätzel, M.; Hagfeldt, A. Highly Efficient Planar Perovskite Solar Cells through Band Alignment Engineering. *Energy Environ. Sci.* **2015**, *8* (10), 2928–2934.

(10) Liu, D.; Kelly, T. L. Perovskite Solar Cells with a Planar Heterojunction Structure Prepared Using Room-Temperature Solution Processing Techniques. *Nat. Photonics* **2014**, *8* (2), 133–138.

(11) Zuo, L.; Gu, Z.; Ye, T.; Fu, W.; Wu, G.; Li, H.; Chen, H. Enhanced Photovoltaic Performance of CH3NH3PbI3 Perovskite Solar Cells through Interfacial Engineering Using Self-Assembling Monolayer. *J. Am. Chem. Soc.* **2015**, *137* (7), 2674–2679.

(12) Ke, W.; Fang, G.; Wan, J.; Tao, H.; Liu, Q.; Xiong, L.; Qin, P.; Wang, J.; Lei, H.; Yang, G.; Qin, M.; Zhao, X.; Yan, Y. Efficient Hole-Blocking Layer-Free Planar Halide Perovskite Thin-Film Solar Cells. *Nat. Commun.* **2015**, *6*, 6700.

(13) Ke, W.; Fang, G.; Liu, Q.; Xiong, L.; Qin, P.; Tao, H.; Wang, J.; Lei, H.; Li, B.; Wan, J.; Yang, G.; Yan, Y. Low-Temperature Solution-Processed Tin Oxide as an Alternative Electron Transporting Layer for Efficient Perovskite Solar Cells. *J. Am. Chem. Soc.* **2015**, *137* (21), 6730–6733.

(14) Ke, W.; Xiao, C.; Wang, C.; Saparov, B.; Duan, H.-S.; Zhao, D.; Xiao, Z.; Schulz, P.; Harvey, S. P.; Liao, W.; Meng, W.; Yu, Y.; Cimaroli, A. J.; Jiang, C.-S.; Zhu, K.; Al-Jassim, M.; Fang, G.; Mitzi, D. B.; Yan, Y. Employing Lead Thiocyanate Additive to Reduce the Hysteresis and Boost the Fill Factor of Planar Perovskite Solar Cells. *Adv. Mater.* **2016**, *28* (26), 5214–5221.

(15) Ke, W.; Zhao, D.; Xiao, C.; Wang, C.; J. Cimaroli, A.; R. Grice, C.; Yang, M.; Li, Z.; Jiang, C.-S.; Al-Jassim, M.; Zhu, K.; G. Kanatzidis, M.; Fang, G.; Yan, Y. Cooperative Tin Oxide Fullerene Electron Selective Layers for High-Performance Planar Perovskite Solar Cells. *J. Mater. Chem. A* **2016**, *4* (37), 14276–14283.

(16) Wang, C.; Zhao, D.; R. Grice, C.; Liao, W.; Yu, Y.; Cimaroli, A.; Shrestha, N.; J. Roland, P.; Chen, J.; Yu, Z.; Liu, P.; Cheng, N.; J. Ellingson, R.; Zhao, X.; Yan, Y. Low-Temperature Plasma-Enhanced Atomic Layer Deposition of Tin Oxide Electron Selective Layers for Highly Efficient Planar Perovskite Solar Cells. *J. Mater. Chem. A* **2016**, *4* (31), 12080–12087.

(17) Liu, X.; Tsai, K.-W.; Zhu, Z.; Sun, Y.; Chueh, C.-C.; Jen, A. K.-Y. A Low-Temperature, Solution Processable Tin Oxide Electron-Transporting Layer Prepared by the Dual-Fuel Combustion Method for Efficient Perovskite Solar Cells. *Adv. Mater. Interfaces* **2016**, *3* (13), 1600122.

(18) Anaraki, E. H.; Kermanpur, A.; Steier, L.; Domanski, K.; Matsui, T.; Tress, W.; Saliba, M.; Abate, A.; Grätzel, M.; Hagfeldt, A.; Correa-Baena, J.-P. Highly Efficient and Stable Planar Perovskite Solar Cells by Solution-Processed Tin Oxide. *Energy Environ. Sci.* **2016**, *9* (10), 3128–3134.

(19) Yang, G.; Lei, H.; Tao, H.; Zheng, X.; Ma, J.; Liu, Q.; Ke, W.; Chen, Z.; Xiong, L.; Qin, P.; Chen, Z.; Qin, M.; Lu, X.; Yan, Y.; Fang, G. Reducing Hysteresis and Enhancing Performance of Perovskite Solar Cells Using Low-Temperature Processed Y-Doped SnO_2 Nanosheets as Electron Selective Layers. *Small* **2017**, *13* (2), 160179.

(20) Bai, Y.; Fang, Y.; Deng, Y.; Wang, Q.; Zhao, J.; Zheng, X.; Zhang, Y.; Huang, J. Low Temperature Solution-Processed Sb:SnO_2 Nanocrystals for Efficient Planar Perovskite Solar Cells. *ChemSusChem* **2016**, *9* (18), 2686–2691.

(21) Jiang, Q.; Zhang, L.; Wang, H.; Yang, X.; Meng, J.; Liu, H.; Yin, Z.; Wu, J.; Zhang, X.; You, J. Enhanced Electron Extraction Using SnO_2 for High-Efficiency Planar-Structure $HC(NH_2)_2PbI_3$-Based Perovskite Solar Cells. *Nat. Energy* **2016**, *2* (1), 16177.

(22) Wojciechowski, K.; Leijtens, T.; Siprova, S.; Schlueter, C.; Hörantner, M. T.; Wang, J. T.-W.; Li, C.-Z.; Jen, A. K.-Y.; Lee, T.-L.; Snaith, H. J. C60 as an Efficient N-Type Compact Layer in Perovskite Solar Cells. *J. Phys. Chem. Lett.* **2015**, *6* (12), 2399–2405.

(23) Jiang, C.-S.; Yang, M.; Zhou, Y.; To, B.; Nanayakkara, S. U.; Luther, J. M.; Zhou, W.; Berry, J. J.; Lagemaat, J. van de; Padture, N. P.; Zhu, K.; Al-Jassim, M. M. Carrier Separation and Transport in Perovskite Solar Cells Studied by Nanometre-Scale Profiling of Electrical Potential. *Nat. Commun.* **2015**, *6*, 8397.

(24) Jiang, C.-S.; Ptak, A.; Yan, B.; Moutinho, H. R.; Li, J. V.; Al-Jassim, M. M. Microelectrical Characterizations of Junctions in Solar Cell Devices by Scanning Kelvin Probe Force Microscopy. *Ultramicroscopy* **2009**, *109* (8), 952–957.

(25) Moutinho, H. R.; Dhere, R. G.; Jiang, C.-S.; Yan, Y.; Albin, D. S.; Al-Jassim, M. M. Investigation of Potential and Electric Field Profiles in Cross Sections of CdTe/CdS Solar Cells Using Scanning Kelvin Probe Microscopy. *J. Appl. Phys.* **2010**, *108* (7), 074503.

(26) Jiang, C.-S.; Moutinho, H. R.; Reedy, R.; Al-Jassim, M. M.; Blosse, A. Two-Dimensional Junction Identification in Multicrystalline Silicon Solar Cells by Scanning Kelvin Probe Force Microscopy. *J. Appl. Phys.* **2008**, *104* (10), 104501.

(27) Yu, Y.; Wang, C.; Grice, C. R.; Shrestha, N.; Chen, J.; Zhao, D.; Liao, W.; Cimaroli, A. J.; Roland, P. J.; Ellingson, R. J.; Yan, Y. Improving the Performance of Formamidinium and Cesium Lead Triiodide Perovskite Solar Cells Using Lead Thiocyanate Additives. *ChemSusChem* **2016**, *9* (23), 3288–3297.

(28) Chueh, C.-C.; Li, C.-Z.; Jen, A. K.-Y. Recent Progress and Perspective in Solution-Processed Interfacial Materials for Efficient and Stable Polymer and Organometal Perovskite Solar Cells. *Energy Environ. Sci.* **2015**, *8* (4), 1160–1189.

(29) Shao, Y.; Yuan, Y.; Huang, J. Correlation of Energy Disorder and Open-Circuit Voltage in Hybrid Perovskite Solar Cells. *Nat. Energy* **2016**, *1* (1), 15001.

(30) Hu, T.; Becker, T.; Pourdavoud, N.; Zhao, J.; Brinkmann, K. O.; Heiderhoff, R.; Gahlmann, T.; Huang, Z.; Olthof, S.; Meerholz, K.; Többens, D.; Cheng, B.; Chen, Y.; Riedl, T. Perovskite Solar Cells: Indium-Free Perovskite Solar Cells Enabled by Impermeable Tin-Oxide Electron Extraction Layers. *Adv. Mater.* **2017**, *29* (27), 1606656.

(31) Zhou, X.; Li, X.; Liu, Y.; Huang, F.; Zhong, D. Interface Electronic Properties of Co-Evaporated $MAPbI_3$ on ZnO(0001): In Situ X-Ray Photoelectron Spectroscopy and Ultraviolet Photoelectron Spectroscopy Study. *Appl. Phys. Lett.* **2016**, *108* (12), 121601.
(32) Olthof, S.; Meerholz, K. Substrate-Dependent Electronic Structure and Film Formation of $MAPbI_3$ Perovskites. *Sci. Rep.* **2017**, *7*, 40267.
(33) Zou, Y.; Meng, Q.; Mao, H.; Zhu, D. Substrate Effect on the Interfacial Electronic Structure of Thermally-Evaporated $CH_3NH_3PbI_3$ Perovskite Layer. *Org. Electron.* **2017**, *41*, 307–314.
(34) Xu, H.; Wu, Y.; Cui, J.; Ni, C.; Xu, F.; Cai, J.; Hong, F.; Fang, Z.; Wang, W.; Zhu, J.; Wang, L.; Xu, R.; Xu, F. Formation and Evolution of the Unexpected PbI_2 Phase at the Interface during the Growth of Evaporated Perovskite Films. *Phys. Chem. Chem. Phys.* **2016**, *18* (27), 18607–18613.
(35) Sites, J. R. Quantification of Losses in Thin-Film Polycrystalline Solar Cells. *Sol. Energy Mater. Sol. Cells* **2003**, *75* (1), 243–251.
(36) Wang, C.; Xiao, C.; Yu, Y.; Zhao, D.; Awni, R. A.; Grice, C. R.; Ghimire, K.; Constantinou, I.; Liao, W.; Cimaroli, A. J.; Liu, P.; Chen, J.; Podraza, N. J.; Jiang, C.-S.; Al-Jassim, M. M.; Zhao, X.; Yan, Y. Understanding and Eliminating Hysteresis for Highly Efficient Planar Perovskite Solar Cells. *Adv. Energy Mater.* **2017**, *7* (17), 1700414.

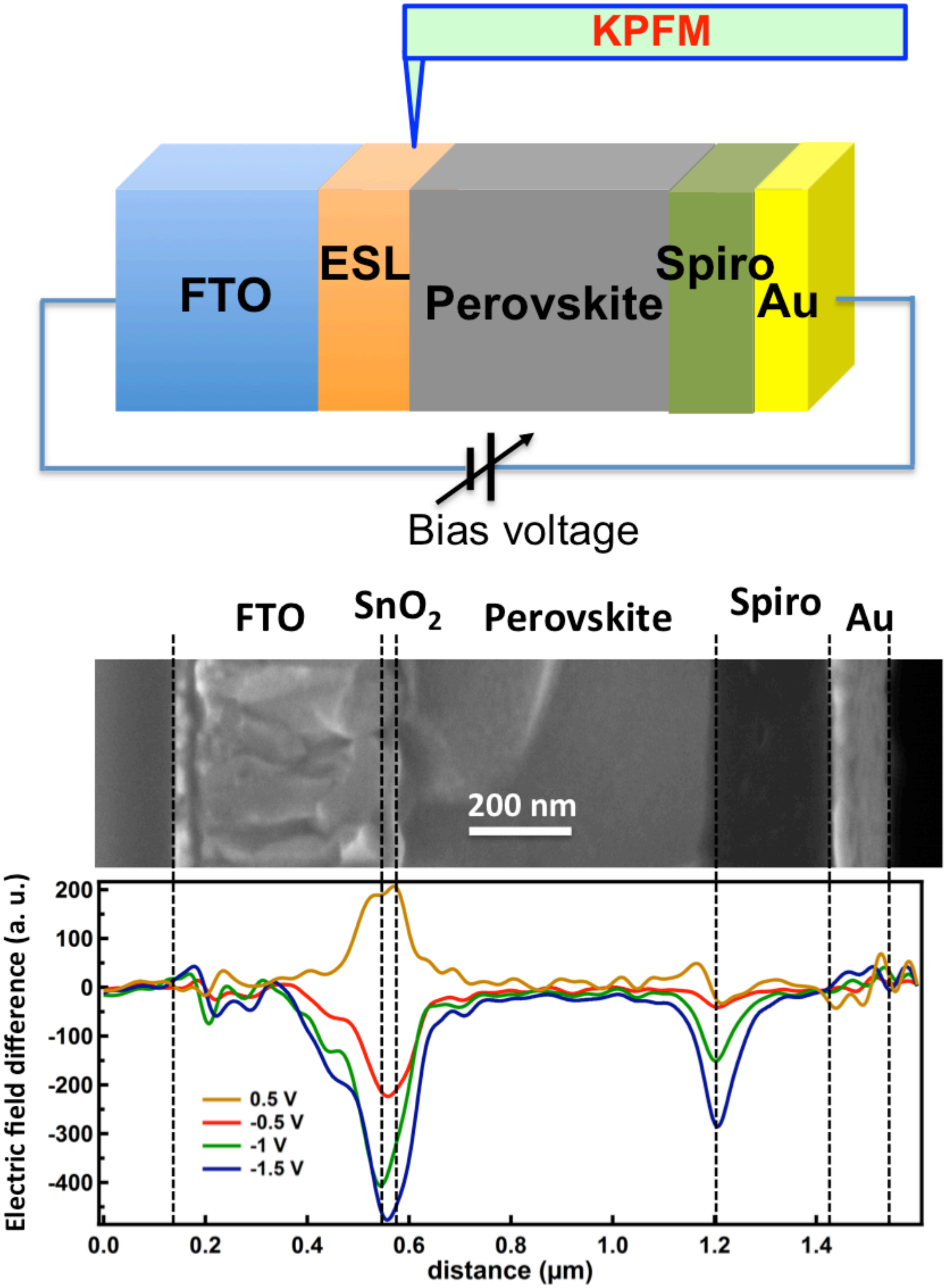
KPFM
FTO
ESL
Perovskite
Spiro
Au
Bias voltage
FTO
SnO_2
Perovskite
Spiro
Au
200 nm
Electric field difference (a. u.)
200
100
0
-100
-200
-300
-400
0.5 V
-0.5 V
-1 V
-1.5 V
0.0
0.2
0.4
0.6
0.8
1.0
1.2
1.4
distance (μm)